

Research Paper

Annealing-modulated nanoscintillators for nonconventional X-ray activation of comprehensive photodynamic effects in deep cancer theranostics

Yao-Chen Chuang^{1*}, Chia-Hui Chu^{1*}, Shih-Hsun Cheng^{1,2}, Lun-De Liao¹, Tsung-Sheng Chu¹, Nai-Tzu Chen³, Arthur Paldino⁴, Yu Hsia¹, Chin-Tu Chen², and Leu-Wei Lo¹✉

1. Institute of Biomedical Engineering and Nanomedicine Research, National Health Research Institutes, 35 Keyan Road, Zhunan 350, Taiwan.
2. Department of Radiology, The University of Chicago, Chicago, IL 60637, USA.
3. Department of Cosmeceutics, China Medical University, 91 Hsueh-Shih Road, Taichung, Taiwan 40402.
4. Faculté de médecine Lyon-Est, Université Claude Bernard, 8 Avenue Rockefeller, Lyon 69008, France.

*These authors contributed equally to this work.

✉ Corresponding author: Leu-Wei Lo, Ph.D., Institute of Biomedical Engineering and Nanomedicine, National Health Research Institutes, Zhunan, Miaoli 35053, Taiwan, Tel: 886-37-246166 # 37115, Fax: 886-37-586440, E-mail: lwlo@nhri.edu.tw.

© The author(s). This is an open access article distributed under the terms of the Creative Commons Attribution License (<https://creativecommons.org/licenses/by/4.0/>). See <http://ivyspring.com/terms> for full terms and conditions.

Received: 2019.11.03; Accepted: 2020.05.04; Published: 2020.05.20

Abstract

Photodynamic therapy (PDT), which involves the generation of reactive oxygen species (ROS) through interactions of a photosensitizer (PS) with light and oxygen, has been applied in oncology. Over the years, PDT techniques have been developed for the treatment of deep-seated cancers. However, (1) the tissue penetration limitation of excitation photon, (2) suppressed efficiency of PS due to multiple energy transfers, and (3) insufficient oxygen source in hypoxic tumor microenvironment still constitute major challenges facing the clinical application of PDT for achieving effective treatment. We present herein a PS-independent, ionizing radiation-induced PDT agent composed of yttrium oxide nanoscintillators core and silica shell ($Y_2O_3:Eu@SiO_2$) with an annealing process. Our results revealed that annealed $Y_2O_3:Eu@SiO_2$ could directly induce comprehensive photodynamic effects under X-ray irradiation without the presence of PS molecules. The crystallinity of $Y_2O_3:Eu@SiO_2$ was demonstrated to enable the generation of electron-hole ($e-h^+$) pairs in Y_2O_3 under ionizing irradiation, giving rise to the formation of ROS including superoxide, hydroxyl radical and singlet oxygen. In particular, combining $Y_2O_3:Eu@SiO_2$ with fractionated radiation therapy increased radio-resistant tumor cell damage. Furthermore, photoacoustic imaging of tumors showed re-distribution of oxygen saturation (sO_2) and reoxygenation of the hypoxia region. The results of this study support applicability of the integration of fractionated radiation therapy with $Y_2O_3:Eu@SiO_2$, achieving synchronously in-depth and oxygen-insensitive X-ray PDT. Furthermore, we demonstrate $Y_2O_3:Eu@SiO_2$ exhibited radioluminescence (RL) under X-ray irradiation and observed the virtually linear correlation between X-ray-induced radioluminescence (X-RL) and the $Y_2O_3:Eu@SiO_2$ concentration *in vivo*. With the pronounced X-RL for *in-vivo* imaging and dosimetry, it possesses significant potential for utilization as a precision theranostics producing highly efficient X-ray PDT for deep-seated tumors.

Key words: Photodynamic therapy; annealing; nanoscintillator; fractionated radiotherapy; X-ray induced radioluminescence; vascular remodeling; radioresistance

Introduction

More than ten million individuals worldwide are diagnosed with cancer annually, and effective technologies for eradicating tumors are urgently needed. Traditional approaches such as surgery,

chemotherapy, radiation therapy, photodynamic therapy (PDT), and hyperthermia have shown great success in widespread clinical and preclinical use. Among those promising approaches, PDT, a

noninvasive and site-directed medical technique based on the destruction of tumor tissues by light inducing reactive oxygen species (ROS) generation, has undergone extensive investigations in recent years. In PDT, a photosensitizer (PS) is activated by a specific wavelength of light to generate ROS or free radicals that can react with the local microenvironment, and eventually results in cell death and tissue devastation [1,2]. In terms of spatial selectivity in PDT, specific targeting of the PS to the tumor compartment by attaching with various targeting ligands is crucial. Tumor specific accumulation followed by local irradiation facilitates targeted damage to malignant tissue while sparing surrounding healthy tissues [3].

To date, the current clinical use of PDT has been limited to superficial layers of tissues, such as in skin cancer, lung cancer, and esophageal cancer that are easily accessible. A major challenge in most traditional PDT is the difficulty in delivering UV or visible light into the subsurface for PS activation. This limits clinical applications of PDT due to the short penetration depth of illumination light, which leads to ineffective treatment of deep-seated tumors [4,5]. One auspicious strategy to overcome the limitation of PDT for deep tumor treatment is the development of novel near-infrared (NIR) PSs or using nanoparticles as PS carriers to establish two-photon PDT or upconversion nanoparticle-mediated PDT [6-9], which aims to minimize tissue interference and improve penetration depth. For example, Cheng et al. showed that the mesoporous silica nanoparticles (MSN) co-encapsulated two-photon absorbing dyes and PS enabled high-energy transfer rates for two-photon activated PDT. The two-photon PDT system enhanced the energy transfer rate up to unprecedented 93% to yield efficacy in deep tissue [10]. In another study by Chen et al., plasmon-enhanced photoluminescence of GNRs induced by two-photon excitation at NIR wavelength demonstrated the intra-particle energy transfer. This phenomenon induced singlet oxygen generation, which is worthy of studying its potential for development in clinical translation [11]. However, even with this advancement, the photon penetration depth can only be increased to a few centimeters into soft tissue [12]. Moreover, reduced $^1\text{O}_2$ generation efficiency has been reported by using NIR-activated PSs, and the efficiency of energy transfer from NP toward the PS has usually limited the clinical use of PDT [8,13].

Many recent alternative approaches have been developed to improve tissue penetration capability of PDT, including microwave [14,15], ultrasound [16] and X-ray [17-19]. Among them, X-ray, with the highest penetration depth, was proposed as an energy

source to interact with scintillating nanoparticles and then activate PDT, which could be termed as X-ray excited PDT (hereinafter called as X-ray PDT). In a pilot study, Chen et al. developed self-lighting PDT, in which nanoparticles upon exposure to extrinsic X-rays emit luminescence in the visible region of the spectrum, activating the attached PS, and resulting in the efficient generation of $^1\text{O}_2$ [20]. Apart from this, the use of photons from Cerenkov radiation (CR) has been emerging as an internal light source to activate PS *in vivo*. Cerenkov luminescence is mainly composed of UV-blue photons, which deliver rapid and localized excitation source for Cerenkov luminescence induced PDT without prolonged radiation exposure to healthy tissue [21]. Even though, remarkable results of cancer eradication *in vitro* and *in vivo* have been observed in recent years [22-24], the investigation, evaluation and application of deep PDT for clinical use are still in its infancy. Much room remains for improving the efficiency of X-ray PDT, including photobleaching of organic PSs during X-ray irradiation [25], PS loading efficiency for maximized $^1\text{O}_2$ production [24,26], matching and fluorescence resonance energy transfer (FRET) efficiency between scintillator and PS [27,28], and illumination fluence and fluence rate [29,30]. Moreover, the hypoxia microenvironment of tumor, either pre-existing or as a result of oxygen depletion during PDT, can significantly decrease the effectiveness of PDT-induced cell killing [8,31,32]. To minimize the hypoxia-limited therapeutic effect in PDT, a circumventive strategy was developed involving a combination of scintillators and inorganic PSs, such as ZnO or TiO_2 . These approaches not only reduced the possibility of PS photodestruction, but also provided a solution to diminish the O_2 -dependence of PDT [33]. Furthermore, in the context of cancer therapy, radiation therapy still plays a critical role in the management of more than 50% of cancer cases. The success of radiation therapy also depends on clinical and radiobiological factors. For example, delivering the dose in single or hypofractionated schedule may increase the therapeutic index of treatment compared to conventionally hyperfractionated radiation therapy. However, hyperfractionated radiation therapy could open temporarily closed blood vessels and result in as short-term local reoxygenation and change cellular radiosensitivity during multifraction delivery [34]. Therefore, the radiation dose is believed to be a double-edged sword in X-ray PDT.

Herein, we reported the development of silica-coated scintillating $\text{Y}_2\text{O}_3:\text{Eu}$ nanoparticles ($\text{Y}_2\text{O}_3:\text{Eu}@\text{SiO}_2$) that undergo annealing treatment could exhibit not only enhanced photoluminescence

efficiency, but also the ability to generate cytotoxic singlet oxygen, superoxide anion and hydroxyl radical upon X-ray irradiation without the incorporation of any additional PS. In this case, the excitation energy is absorbed first by the host lattices, and the electrons (e^-) of NPs are promoted across the band gap to the conduction band, which creates a hole (h^+) in the valence band. We observed that ROS generation may result from electrons in the conduction band and holes in the valence band that exhibit high reducing and oxidizing power, respectively. We further implemented a fractionated radiation regimen with $Y_2O_3:Eu@SiO_2$ to explore an approach relevant to clinical conventionally fractionated radiation therapy. By comparing radio-sensitive (CAOV3) and radio-resistant (SKOV3) ovarian cancer cells, our established annealing-modulated $Y_2O_3:Eu@SiO_2$ could improve the radiotherapy efficacy of CAOV3 cells by means of ROS generation and inducing reoxygenation to overcome tumor hypoxia. Our work demonstrated that the as-synthesized $Y_2O_3:Eu@SiO_2$ had potential applications in X-ray PDT with RL-visualized nanodosimetry to overcome the radio-resistant cancers.

Experiment section

Chemicals and materials

$Y(NO_3)_3$, $Eu(NO_3)_3$, urea, tetraethylorthosilicate (TEOS), ammonium hydroxide (30%), and ethanol were purchased from Acros. Diphenolbenzofuran (DPBF), dihydroethidium (DHE), coumarin-3-carboxylic acid (3-CCA), and 5-tertbutoxycarbonyl-5-methyl-1-pyrroline N-oxide (BMPO) were obtained from Sigma Chemical Co. Propidium Iodide (PI) and YO-PRO-1 was purchased from Invitrogen. All chemicals were used as received without further purification.

Synthesis of $Y_2O_3:Eu@SiO_2$ nanoparticles

In a typically synthetic procedure via the urea homogeneous precipitation method [35], $0.04 \text{ mol}\cdot\text{L}^{-1}$ $Y(NO_3)_3\cdot 6H_2O$, $0.002 \text{ mol}\cdot\text{L}^{-1}$ $Eu(NO_3)_3\cdot 6H_2O$, and $2 \text{ mol}\cdot\text{L}^{-1}$ urea were mixed together, and then aged for 4 h at 85°C . Then, the light-white precursors were collected by centrifugation, washed repeatedly with deionized water, and then dried in an oven at 60°C . The precursor of $Y_2O_3:Eu$ was obtained after drying this product at 80°C for 12 h. Coating of SiO_2 was carried out by hydrolysis of tetraethoxysilane (TEOS) [34]. Firstly, 250 mg of $Y_2O_3:Eu$ NPs was dispersed in 100 mL ethanol by sonication for 15 min, and then mixed with 1 mL ammonia (25 wt% purity) with vigorous stirring. Then 0.6 mL TEOS was then added

dropwise to the solution. After stirring at room temperature for 1.5 h, the resultant products were washed several times with ethanol and water, and the as-synthesized materials were dried at 60°C , and then sintered at 800°C in air for 4 h.

Characterization

Particle morphology of $Y_2O_3:Eu$ and $Y_2O_3:Eu@SiO_2$ samples was characterized via transmission electron microscope (TEM, Hitachi, H-7650 operating at an acceleration voltage of 80 kV). The excitation sources for the X-ray photoluminescence spectra and X-ray excited optical imaging were the intensity modulated radiotherapy system at the University of Chicago. The irradiator was operating in the range from 40 to 225 kV acceleration potential (no Cu filter), 1~25 mA tube current, and a 15 mm diameter collimator. The emission spectra were recorded using fiber optic cables connected to a fluorescence spectrometer (USB 4000) from Ocean Optics. For the optical imaging, 10 mg of $Y_2O_3:Eu@SiO_2$ nanoparticles was packed into a 1.6 mm ID borosilicate glass tube phantom. The phantom was irradiated with the 140 kV / 20.89 mA, a 15 mm diameter collimated X-ray source, and imaging was performed by a Canon 5D Mark II with Canon 35 mm lens, F 1.4 L (stopped down to F 8.0).

Reactive oxygen species (ROS) detection in solution

For the quantification of ROS, three specific species, i.e., singlet oxygen (1O_2), superoxide anion ($O_2^{\cdot-}$), and hydroxyl radical ($\cdot OH$), were chosen for their biological importance. Generation of these species was measured by three kinds of probes, DPBF (absorbance: 402 nm) and 3-CCA (excitation: 395 nm, emission: 450 nm) were dedicated to the quantification of integrated amounts of 1O_2 , and $\cdot OH$, respectively. Both of DHE and BMPO were assigned to the quantification of $O_2^{\cdot-}$ [37-39]. Two hundred and fifty micrograms of $Y_2O_3:Eu@SiO_2$ was suspended with 1 mL PBS for ROS measurement. ROS probe was premixed with $Y_2O_3:Eu@SiO_2$ and then diluted by PBS for the designed final concentration. The resulting final concentrations of DPBF, DHE, and 3-CCA were 40 μM , 10 μM and 25 μM , respectively. Solutions were then exposed to X-rays by using a commercial cabinet X-ray system with the standard X-ray tube operated at 150 kV and 15 mA. Singlet oxygen measurements were made by following the loss of UV absorbance of DPBF in the aqueous $Y_2O_3:Eu@SiO_2$ solutions. In the DHE measurement, the solution was excited at 465 nm, and its fluorescence intensity at 585 nm was measured. In the BMPO measurement, the

characteristic spectrum of BMPO/ \bullet OH adduct ($a^N = 13.56$, $a^P_H = 12.30$, and $a^V_H = 0.66$) was measured.

Phantom preparation and calibration curve establishment

Intralipid, with a refractive index close to soft tissue and negligible absorption in visible spectral region has been widely used as tissue-mimicking phantom. Intralipid phantoms were prepared according to the literature [38]. Briefly, 2.5 g of type A gelatin was added to 50 mL of deionized water, then the mixture was heated to a temperature above the gelatin's melting point until the gelatin dissolved completely and the solution turned transparent. Subsequently, 0.5 g of intralipid and various concentrations of $Y_2O_3:Eu@SiO_2$ were added into the gelatin-water solution followed by filling cylindrical molds with the final solution, and let the hydrogel solidify at room temperature. For constructing the calibration curve, an imaging system was established; consisting of an X-ray source (RS-2000, Rad Source Co., Ltd) positioned approximately 20 cm above the intralipid phantom, and a CCD camera module placed perpendicularly to the irradiation source and 30 cm away from the phantom. Black curtains were used to darken the imaging space. Acquired X-RL images were further processed using MATLAB.

In vivo radioluminescence imaging

For RL studies, nude mice were anesthetized with isoflurane (1.5~2% inhalation), and the SKOV3 human ovarian cells (5×10^6 cells in 0.2 mL PBS) were subcutaneously injected into right flanks of the mice. When the tumors reached approximately 500 mm³, tumors were intratumoral injected with different concentration of $Y_2O_3:Eu@SiO_2$ and imaged after 1 h using the homemade radioluminescence system operating at 160 kVp and 5 mA. At the end of the study when the survived mice were sacrificed, all tumors in each study group were measured by ICP-MS to quantify the concentration of $Y_2O_3:Eu@SiO_2$. All mice were anesthetized with an intraperitoneal injection of a ketamine hydrochloride and xylazine cocktail prior to imaging.

Cell culture

SKOV3 (human ovarian cancer) and CAOV3 (human ovarian cancer) cell lines were purchased from American Tissue Culture Collection (ATCC). SKOV3 and CAOV3 cells were cultured in McCoy's 5A (Gibco) and DMEM (Gibco), respectively. All cell lines were incubated at 37 °C in a fully humidified atmosphere of 5% CO₂.

In vitro confocal images of cytotoxicity of $Y_2O_3:Eu@SiO_2$ and radiotherapy effects

To determine the *in vitro* radiotherapy effects, SKOV3 and CAOV3 ovarian cancer cells were cultured in McCoy's 5A and DMEM medium containing 10% fetal bovine serum (FBS) at 37 °C under 5% CO₂. Cells were seeded at a density of 3×10^4 on a 60 mm dish to permit cell attachment. Until 80% cell density, the cells were carefully washed with phosphate-buffered saline (PBS), refreshed with fresh medium containing 50 μ g mL⁻¹ of $Y_2O_3:Eu@SiO_2$, and then incubated at 37 °C and 5% CO₂ for 3h or 24 h. After incubation, the cells were rinsed with PBS three times to remove the excess nanoparticles and placed in fresh medium that contained YOPRO-1 and PI dyes. The cell nuclei were stained with 1 μ M Hoechst 33342 for 10 min and washed three times with PBS. For cell morphology and fluorescence imaging, YOPRO-1 was excited at 488 nm and monitored using a 525 ± 5 nm bandpass filter, while PI was excited at 535 nm and monitored using a 620 ± 5 nm bandpass filter. Images were collected using a confocal microscope (Zeiss LSM 710).

Cytotoxicity in vitro

The cytotoxic effect of the $Y_2O_3:Eu@SiO_2$ was determined by a standard MTT assay in 96 well plates. Approximately 5×10^3 cells were placed in each well and cultured at 37 °C with 5% CO₂. After 24 h of incubation, the media were removed and replaced with fresh medium supplemented with 10% FBS containing $Y_2O_3:Eu@SiO_2$ at concentrations ranging from 0 μ g mL⁻¹ to 100 μ g mL⁻¹. After 24, the medium containing $Y_2O_3:Eu@SiO_2$ was replaced by 180 μ L fresh medium, followed by the addition of 20 μ L MTT. After 4 h of culturing, the medium was substituted with DMSO (150 μ L); the survival rate was evaluated via absorbance measurements at 570 nm.

Clonogenic assay

Appropriate cell numbers were plated for survival analysis. Culture medium was removed and replaced with nanoparticle-containing culture medium for 24 h at 37 °C. Radiation was delivered in a single dose of 1~2 Gy over an appropriate field size at 150 keV and 250 keV, respectively. After irradiation, cells were harvested, counted, and seeded on a 100 mm dish. Cell cultures were then incubated for 10-14 days at 37 °C in 5% CO₂ in air and 95% humidity. Colonies are fixed with glutaraldehyde (6.0% v/v), stained with crystal violet (0.5% w/v), and counted with each experiment performed in quadruplicate.

In vivo radiotherapy combined with X-ray activated PDT effect

All experiments that involved animals were performed in accordance with the guide for the care and use of laboratory animals and approved by the Institutional Animal Care and Use Committee of National Health Research Institutes. *In vivo* experiments were conducted using five to six-week-old female nude mice (BioLASCO Taiwan Co., Ltd.). The mice were anesthetized with isoflurane (1.5~2% inhalation), and the SKOV3 human ovarian cells (5×10^6 cells in 0.2 mL PBS) were subcutaneously injected into right flanks of the mice. The tumors were allowed to reach approximately 500 mm³ in volume estimated with the formula $1/2 (L \times W^2)$, where L and W were the length and width, respectively. The mice were randomized to various treatment groups: control (n=6), Y₂O₃:Eu@SiO₂ (16 mg/kg, n = 6), radiation (total 8 Gy; four fractions of 2 Gy every day, n = 6), and combination (n=6). In the group of combined treatment, 0.1 mL of 16 mg/kg Y₂O₃:Eu@SiO₂ solution was administered to each mouse *via* multipoint intratumoral injection. After 1 h post-injection, the tumors in mice were irradiated using an X-ray irradiator (RS-2000, Rad Source Co., Ltd). Tumor volume observations were measured by caliper twice per week. For each group, immunohistochemical analyses were performed on tumors collected 5 d post-injection and end of experiment.

Measurement of oxygen distribution by photoacoustic imaging

To measure the oxygen saturation (sO₂) inside the SKOV3 solid tumor, the PA C-scan (i.e., two-dimensional scanning) was performed to acquire functional and reference images. Before and after intratumoral administration of 1 mg of Y₂O₃:Eu@SiO₂ and treated with 8 Gy X-ray (four fractions of 2 Gy every day), sO₂ around the tumor was measured at the end of radiation therapy by the differential optical absorption of oxygenated, deoxygenated hemoglobin and total hemoglobin at different wavelengths of 850 nm, 750 nm and 800, respectively. To facilitate comparison of sO₂ patterns at different groups, the regions of interest (ROI) in tumor were employed in the proximity of reagents' injection site, and identified using ultrasound imaging. Photoacoustic B-scans of the mice generating average oxygenated and deoxygenated hemoglobin signals were analyzed by custom-developed software based on MATLAB® (R2007a, The MathWorks, USA), and sO₂ is defined as $sO_2 = [HbO_2] / [HbO_2] + [Hb]$.

Dual-color immunofluorescent analysis of tumors

The therapeutic effects were determined by active caspase-3 and Annexin V immunostaining. The cryosections of tumor tissue collected from 5 d post-injection (5 μm thick) were washed three times, with PBS for 5 min and fixed with freshly prepared 4% paraformaldehyde in PBS, for 15 min at room temperature. The sections were probed overnight with a polyclonal rabbit anti-mouse active caspase-3 antibody (GeneTex) and rabbit anti-mouse Annexin V (GeneTex) at 4 °C, followed by incubation with peroxidase-conjugated polyclonal goat anti-rabbit antibodies IgG (DyLight488) (GeneTex) and goat anti-rabbit IgG (Alex Fluor594) for 1 h, at room temperature. The sections were counterstained with Hoechst 33342 for 30 min and mounted with glass coverslips. The tissue sections were then analyzed by fluorescence microscopy.

The cryosections of tumor tissue collected from end of experiment (5 μm thick) were fixed with freshly prepared 4% paraformaldehyde in PBS, for 15 min at room temperature and washed 3 times with PBS. The sections were probed overnight with mouse anti-CD31 antibody (GeneTex) and rabbit anti-αSMA antibody (GeneTex) at 4 °C, followed by incubation with polyclonal goat anti-mouse IgG (DyLight488) antibodies and polyclonal goat anti-rabbit IgG (DyLight594) antibodies (GeneTex) for 1 hour, at room temperature. The sections were counterstained with Hoechst 33342 for 30 min and mounted with glass coverslips. The tissue sections were then analyzed by fluorescence microscopy and quantified by ImageJ software.

Results and discussion

The low-temperature reflux method, utilizing urea-assisted precipitation, was employed to systematically synthesize nanocrystal compositions. The morphology of calcined Y₂O₃:Eu was characterized by TEM and is shown **Figure 1A**. From the image, it can be observed that the naked Y₂O₃:Eu nanoparticles appeared as homogeneous and monodisperse nanospheres with an average size of 160 nm. For biological applications, water solubility is critical. Coating Y₂O₃:Eu with SiO₂ is the most popular strategy to increase the water solubility of nanoparticles. Additionally, since the induced luminescence could be quenched by water and organic molecules *via* a mechanism similar to fluorescence resonance energy transfer (FRET), SiO₂ could decrease non-radiative transition to prevents the quenching of luminescence quenching [41,42]. Therefore, the Y₂O₃:Eu nanoparticles were coated with a thin layer of silica using the modified Stöber method

and the core-shell structure for the $\text{Y}_2\text{O}_3:\text{Eu}@/\text{SiO}_2$ can be clearly seen due to the different electron penetrability for the cores and shells (as shown in **Figure 1B**). The $\text{Y}_2\text{O}_3:\text{Eu}$ cores are black spheres with an average size of 160 nm, and the shells have a gray color with an average thickness of 9 nm. It was reported by Liu and colleagues that silica-based nanoparticles with size between 100 and 200 nm own the best efficiencies of the cellular uptake and endosomal escape [43,44]. In addition, the coating thickness of outer silica layer has some effect on ROS generation. Due to the extremely short lifespan and severely limited diffusion distance (< 20 nm), ROS only acts in its immediate vicinity. To strike the balance between ROS generation and biocompatibility, a thin silica-layer (<10 nm) was used in our study. **Figure 1C** shows the EDX spectra of $\text{Y}_2\text{O}_3:\text{Eu}@/\text{SiO}_2$. It is explicitly shown from **Figure 1C** that Y, Eu, and Si peaks are at normal energies, which indicates that the composition of coated layer is SiO_2 . The TEM and EDS results as described above confirm the uniform coating of silica shell on our synthesized $\text{Y}_2\text{O}_3:\text{Eu}@/\text{SiO}_2$ nanoparticles. Following synthesis, the optical properties of $\text{Y}_2\text{O}_3:\text{Eu}@/\text{SiO}_2$ nanoparticles were thoroughly characterized. A typical RL spectrum of an aqueous suspension of $\text{Y}_2\text{O}_3:\text{Eu}@/\text{SiO}_2$ nanoparticles under X-ray irradiation is shown in **Figure 1D**. The complete RL spectra were collected and subsequently curve-fitted (Gaussian), and exhibited the characteristic luminescence bands at 590 nm, 610 nm, and 627 nm, which can be assigned to $^5\text{D}_0$

$\rightarrow ^7\text{F}_1$, $^5\text{D}_0 \rightarrow ^7\text{F}_2$, and $^5\text{D}_0 \rightarrow ^7\text{F}_3$ transitions of the Eu^{3+} ion, respectively, indicating that Eu^{3+} sites act as luminescence centers. Based upon the findings in the extant literature, the spectral properties of our RL spectrum of $\text{Y}_2\text{O}_3:\text{Eu}@/\text{SiO}_2$ nanoparticles appear essentially similar to those that were recorded under either UV excitation or X-ray irradiation [45,46].

We have compared photoluminescence and ROS generation efficiency between annealed and pre-annealed nanoparticles. Both photoluminescence and ROS generation of pre-annealed $\text{Y}_2\text{O}_3:\text{Eu}$ nanoparticles are significantly weaker than those of annealed $\text{Y}_2\text{O}_3:\text{Eu}$ nanoparticles (data not shown), the results are in consistent with previous reports. The precursor $(\text{Y}(\text{OH})\text{CO}_3 \cdot \text{H}_2\text{O}):\text{Eu}^{3+}$ nanoparticles contains many hydroxyl groups and is either amorphous or paracrystalline. Due to the defects produced during the preparation process and impurities contained in the raw materials, the samples inevitably have quenching centers (traps), which induce non-radiative transitions and decrease the photoluminescence and ROS generation efficiency. Therefore, a calcination process is indispensable for dehydroxylation and crystallization [47-49]. We next investigated X-RL imaging and radio-sensitization of different Eu doping concentrations to determine if there is an Eu-dependent effect. First, the dependence of RL intensity from Eu^{3+} content was measured, as showed in **Figure 2A**. It is observed that the relative intensity of 610 nm X-RL first increased up to 2 mol% of Eu^{3+} concentration, and then decreased while Eu^{3+}

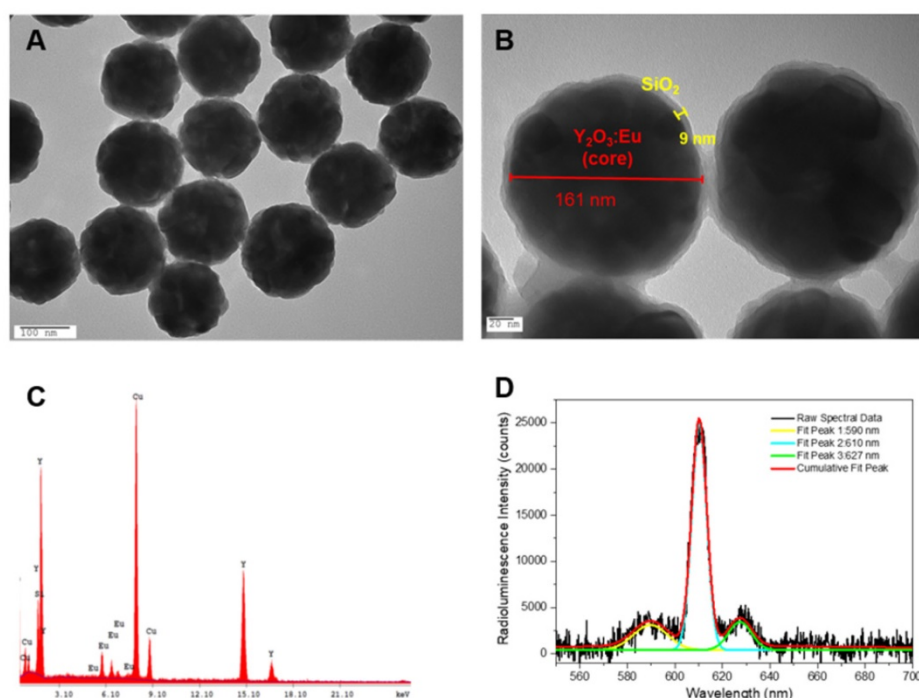


Figure 1. Characterization of $\text{Y}_2\text{O}_3:\text{Eu}@/\text{SiO}_2$. TEM images of (A) $\text{Y}_2\text{O}_3:\text{Eu}$ and (B) $\text{Y}_2\text{O}_3:\text{Eu}@/\text{SiO}_2$; (C) EDX analysis of $\text{Y}_2\text{O}_3:\text{Eu}@/\text{SiO}_2$ particles, and (D) Typical radioluminescence spectra showing dominant emission peaks at 590, 610 nm, and 627 nm, as well as their corresponding, independent Gaussian curve-fits.

dopant concentration continuously increased. This decrease of X-RL as the doping Eu^{3+} level higher than 2 mol % should be resulting from the concentration dependent quenching caused by the cross-relaxation between neighboring Eu^{3+} ions [50,51]. Thus, the optimal concentration of Eu^{3+} ions in our prepared $\text{Y}_2\text{O}_3:\text{Eu}@\text{SiO}_2$ is 2 mol% at the time of synthesis. Scintillators are generally capable of converting high-energy X-rays and gamma rays into UV-visible lights. Limited investigations exist on ROS generation from scintillators. In the case of X-ray inducible PDT, energy transfer may occur if a significant overlap exists between the emission of the donor and the absorption of the acceptor. In order to elucidate the ROS generation mechanism in our study, the contribution of Eu^{3+} concentration to the enhanced generation of hydroxyl radical under X-ray irradiation was estimated by electron paramagnetic resonance (EPR) spectrum (Figure 2B). In the case in which $\text{Y}_2\text{O}_3:\text{Eu}@\text{SiO}_2$ was mixed with BMPO under X-ray irradiation, the EPR revealed a four-line spectrum which implied an $\text{BMPO}\cdot\text{OH}$ adduct [52]. It is worth noting that as shown in Figure 2C, the intensities of $\text{O}_2^{\cdot-}/\cdot\text{OH}$ EPR signals for the as-prepared particles with various Eu^{3+} doping concentrations showed no significant difference. Thus, we do not expect a dominant contribution of Eu^{3+} ions to the ROS generation process under X-ray excitation. At the same time, the RL of $\text{Y}_2\text{O}_3:\text{Eu}@\text{SiO}_2$ was also observed in the absence of O_2 , as shown in

Figure 2D. Moreover, no significant RL variation was found between the normal and O_2 ablation conditions, which indicated that implied RL in our established system is an O_2^- systems, and thus $\text{Y}_2\text{O}_3:\text{Eu}@\text{SiO}_2$ could be employed in image-guided radiotherapy.

PDT allows the destruction of tumors by generating more reactive oxygen species, most often by the singlet oxygen via type II reaction. Herein, the contribution of $\text{Y}_2\text{O}_3:\text{Eu}@\text{SiO}_2$ to the enhanced generation of singlet oxygen production under X-ray irradiation was quantified by measuring the decrease in the optical absorption at 420 nm of $\text{Y}_2\text{O}_3:\text{Eu}@\text{SiO}_2$ nanoparticles suspended in DPBF. Figure 3A illustrates the photobleaching of DPBF in H_2O in the presence of $\text{Y}_2\text{O}_3:\text{Eu}@\text{SiO}_2$ nanoparticles as a function of X-ray dose, relative to a pristine DPBF control (nanoparticle-free) solution. The decrease of DPBF absorption with X-ray dose in the $\text{Y}_2\text{O}_3:\text{Eu}@\text{SiO}_2$ nanoparticle suspension reflects the efficient generation of highly reactive $^1\text{O}_2$. Recently, some groups reported that silica coating enhanced luminescent intensity and suspensibility of Eu-doping phosphor [53-55]. However, with a thick silica layer, the efficiency of the radio-sensitizer may be reduced because it is difficult for reactive singlet oxygen species to diffuse out of the silica layer [56]. In our study, the result demonstrated that there was no obvious effect in the sensitization enhancement under thin silica coating.

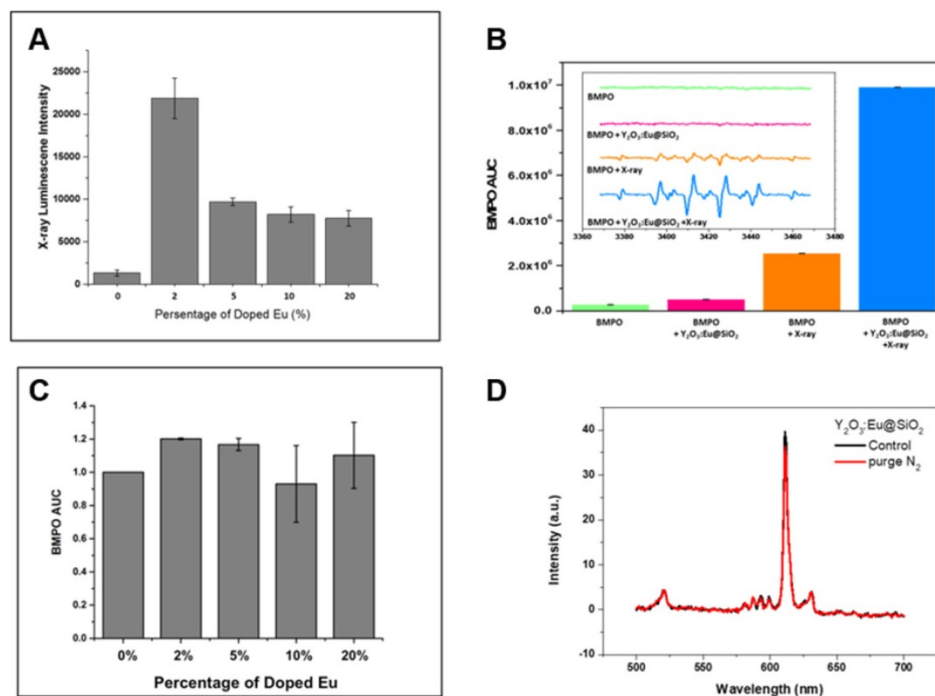


Figure 2. RL and $\text{O}_2^{\cdot-}/\cdot\text{OH}$ generation variation at different conditions. (A) Emission spectrum $\text{Y}_2\text{O}_3:\text{Eu}@\text{SiO}_2$ with different Eu^{3+} ; (B) concentration demonstration of superoxide anion/hydroxyl radical enhanced by $\text{Y}_2\text{O}_3:\text{Eu}@\text{SiO}_2$ under ionizing irradiation; (C) Relative ESR intensity $\text{Y}_2\text{O}_3:\text{Eu}@\text{SiO}_2$ with different Eu^{3+} concentration. (D) Emission spectra of $\text{Y}_2\text{O}_3:\text{Eu}@\text{SiO}_2$ nanoparticle before (black) and after bubbling N_2 gas (red).

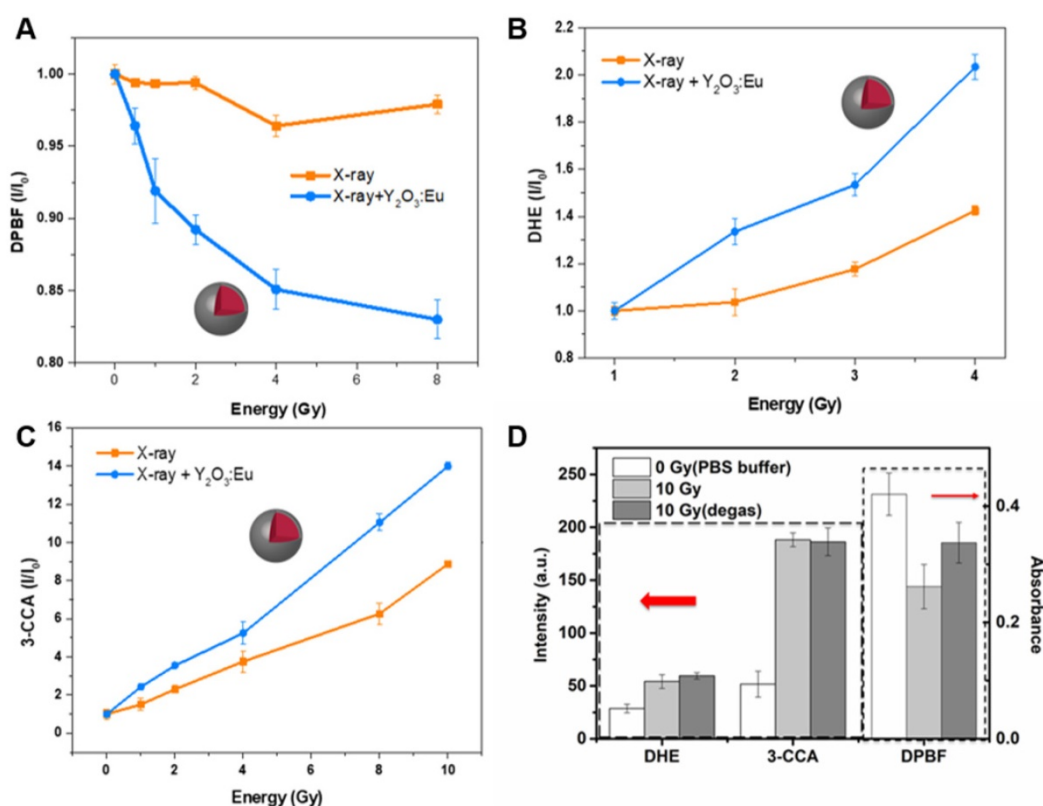


Figure 3. ROS generation kinetics of Y₂O₃:Eu@SiO₂ as a function of X-ray absorbed energy. (A) ¹O₂ measured by DPBF; (B) O₂^{•−} measured by DHE; and (C) •OH measured by 3-CCA. (D) ROS generation of Y₂O₃:Eu@SiO₂ before (light grey) and after bubbling N₂ gas (dark grey) with 10 Gy X-ray. The samples of Y₂O₃:Eu@SiO₂ without X-ray irradiation is as control group (checked).

Besides singlet oxygen, other biologically important reactive oxygen species (ROS), such as •OH and O₂^{•−}, were also characterized during the X-ray excitation of Y₂O₃:Eu@SiO₂ nanoparticles. The DHE is highly sensitive to O₂^{•−} and responses increased as the X-ray absorbed energy. As shown in **Figure 3B**, only Y₂O₃:Eu@SiO₂ yielded a considerable amount of O₂^{•−} under X-ray irradiation. Furthermore, we employed 3-CCA as a trapper to determine whether hydroxyl radical generation can be enhanced by irradiated Y₂O₃:Eu@SiO₂. From the result shown in **Figure 3C**, one can clearly observe the enhanced generation of •OH that arises from the presence of Y₂O₃:Eu@SiO₂ nanoparticles as a function X-ray irradiation dose. Furthermore, it was statistically determined that the ¹O₂, O₂^{•−}, and •OH generations were enhanced by 8.0, 5.4 and 1.6-fold, respectively, in use of Y₂O₃:Eu@SiO₂ mediated X-ray PDT.

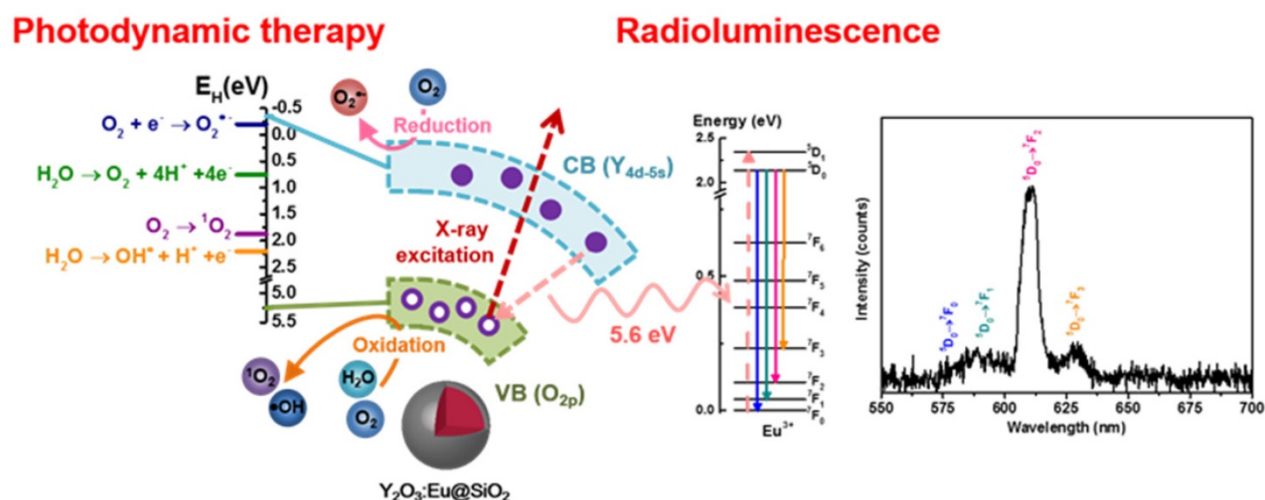
In previous investigations, metallic materials with a high atomic number (Z), such as gold nanoparticles have been demonstrated to enhance photoelectric and Compton effects (and thus the subsequent emissions of secondary electrons) to augment radiation therapy efficacy. However, there are only limited investigations on ROS generation from scintillators. Y₂O₃ was shown to be an effective scintillator that procures self-trapped excitons at

defect sites within the bulk matrix under X-ray irradiation. The incident X-ray photons promote electronic transitions from the valence band to the conduction band and create holes (h⁺) with oxidizing power in the valence band, and electrons (e[−]) with reducing power in the conduction band, respectively [57,58]. In this work, the contribution of annealing-treated Y₂O₃:Eu@SiO₂ to the enhanced generation of a specific type of ROS (e.g., •OH, O₂^{•−} and ¹O₂) could be related to the electronic structures of the Y₂O₃:Eu@SiO₂ nanoparticles, as well as the redox potentials (E_H) of the different ROS generation reactions. Specifically, upon X-ray illumination, a part of energy could transfer from Y₂O₃ nanoscintillators to the Eu³⁺ optical center for fluorescence emission; another part of X-ray energy would be imparted to generate electron-hole pairs (**Scheme 1**). The photoexcited electrons and holes then react with an aqueous electron acceptor (i.e., molecular oxygen) and donor (i.e., water and hydroxyl ions), respectively, to produce different types of ROS. In a previous study, Li and coworkers reported that ROS generation reactions are thermodynamically favorable and predictable by aligning valance band (E_v), conduction band (E_c), and E_H, and vice versa [59]. As has been demonstrated in previous research, the band gap of Y₂O₃ is 5.6 eV, and the theoretical E_v and E_c were 5.25

eV and -0.35 eV, respectively [60]. As shown in **Figure 3**, our experimental results indicated that $\text{Y}_2\text{O}_3:\text{Eu}@\text{SiO}_2$ generated more $\text{O}_2^{\cdot-}$ than the control alone. This suggests that, since the E_c value of Y_2O_3 (-0.35 eV) is lower than the E_H of $\text{O}_2/\text{O}_2^{\cdot-}$ (-0.2 eV), electrons could transfer from Y_2O_3 to O_2 and drive superoxide anion generation. Similarly, the E_H for $\cdot\text{OH}$ and $^1\text{O}_2/\text{O}_2$ generation is approximately 2.2 eV and 1.8 eV, respectively. This means that the holes of Y_2O_3 ($E_v = 5.25$ eV) could theoretically oxidize H_2O into $\cdot\text{OH}$, and drive $^1\text{O}_2$ production in Y_2O_3 solution. It is noteworthy that, unlike conventional PDT that is dependent on the availability of oxygen concentration for Type II reaction, our established PDT effect comprises both Type II energy transfer (oxygen-dependent) and Type I redox reactions (oxygen-independent), and thus minimizes the impediment imposed by the tumor hypoxia on PDT. To further evidence this claim and investigate forms of induced ROS, $\text{Y}_2\text{O}_3:\text{Eu}@\text{SiO}_2$ responses to the absence of O_2 gas were monitored using different indicators for specific ROS inductions following X-ray irradiation. As shown in **Figure 3D**, a pronounced decrease of singlet oxygen was observed after O_2 deprivation under ambient temperature. By contrast, no significant reductions were found in hydroxyl radical and superoxide anion generations in the absence of O_2 . Given the observations, $\text{Y}_2\text{O}_3:\text{Eu}@\text{SiO}_2$ produces comprehensive X-ray activated photodynamic reactions that encompass $^1\text{O}_2$, hydroxyl radical, and superoxide anion, implicating its highly potential utility in PDT for hypoxic cancers.

In order to investigate the use of $\text{Y}_2\text{O}_3:\text{Eu}@\text{SiO}_2$ for biomedical X-ray excited optical luminescence (XEOL) imaging applications, a cabinet irradiator unit was outfitted with a detector positioned perpendicular to a light-tight imaging space (**Figure**

4A). To determine the temporal resolution of the X-RL imaging system, RL from 0.1 to 3 mg of $\text{Y}_2\text{O}_3:\text{Eu}@\text{SiO}_2$ in 10% gelatin with 1% intralipid phantom were captured under various detector exposures following X-ray irradiation (**Figure 4B**). Next, to confirm the practical application of X-RL of $\text{Y}_2\text{O}_3:\text{Eu}@\text{SiO}_2$, various concentrations of $\text{Y}_2\text{O}_3:\text{Eu}@\text{SiO}_2$ were i.t injected into the back flanks tumor of the mice. Anesthetized mice were imaged over 10 s using our custom X-RL imaging system operating under 160 kVp and 5 mA. RL emissions from the 1 mg $\text{Y}_2\text{O}_3:\text{Eu}@\text{SiO}_2$ inclusion were clearly detectable from the injection site (**Figure 4C**). In order to test the feasibility of our proposed method in real samples, the mice were sacrificed, and the unknown concentrations of $\text{Y}_2\text{O}_3:\text{Eu}@\text{SiO}_2$ in different tumors were analyzed using ICP-MS. The analytical results are shown in **Table 1**. The results obtained with X-RL imaging were in good agreement with those obtained by using the ICP-MS method, with a relative error of less than 10%, except 1 mg of $\text{Y}_2\text{O}_3:\text{Eu}@\text{SiO}_2$. These results demonstrate that our proposed method in this work is applicable for real-time detection in *in vivo* study. As shown in **Figure 3**, we have demonstrated that the ability of ROS generation of $\text{Y}_2\text{O}_3:\text{Eu}@\text{SiO}_2$ is independent of europium dopant ion concentration. In addition, in consideration of lanthanide ions are close in ionic radius to yttrium (for example, 1.933 \AA for Yb, 1.761 \AA for Er and 1.8 \AA for Y), the lanthanide ions could be incorporated into the Y_2O_3 host without significant lattice distortions. It implicated that we could replace europium with other rare-earth elements (such as Yb^{3+} and Er^{3+}), so to shift the corresponding radioluminescences toward longer wavelengths for better tissue penetration.



Scheme 1. Plot for potential mechanism of ROS generation and radio-luminescence (RL) in $\text{Y}_2\text{O}_3:\text{Eu}@\text{SiO}_2$.

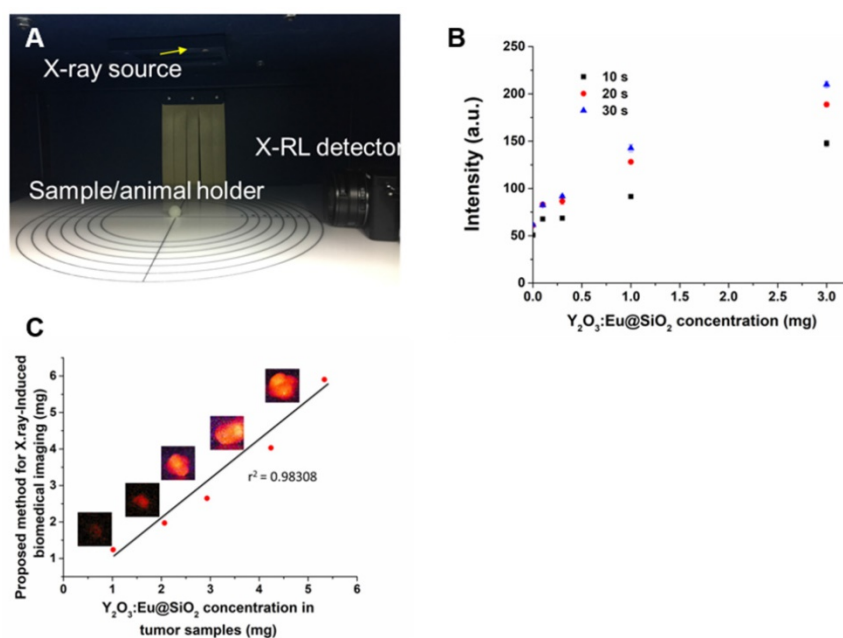


Figure 4. X-RL image for deep tissue imaging activated by X-ray. (A) X-RL imaging system consists of a highly sensitive X-RL detector (CCD camera) and X-ray irradiator cabinet is enclosed within a light tight environment. (B) Exposure sensitivity of the X-RL imaging system was assessed by exciting $Y_2O_3:Eu@SiO_2$ phantoms under 160 kVp X-rays. (C) The in-vivo calibration curve of X-RL intensity vs. particle concentration using subcutaneously inoculated SKOV3 tumor model.

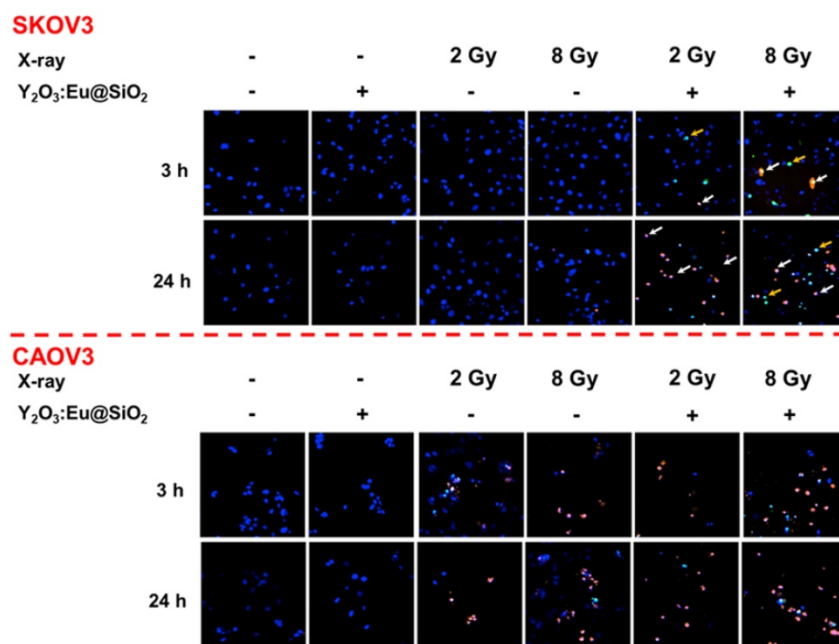


Figure 5. X-ray PDT induced cellular damage in ovarian cells. Confocal fluorescence microscopy images showing the radiotherapy performance of radioresistant SKOV3 (upper) and radiosensitive CAOV3 (bottom) cancer cells. YO-PRO-1 (green) and propidium iodide (PI) signals (red) denote leakage of the cell and nuclear membranes, respectively. The accumulative $Y_2O_3:Eu@SiO_2$ enhanced the ROS generation and increased frequencies of early apoptosis (yellow) and necrosis (white).

Table 1. Comparison of $Y_2O_3:Eu@SiO_2$ concentrations measured using ICP-MS and X-RL in subcutaneously inoculated SKOV3 tumor model

Sample No.	ICP-MS	Proposed method ^a	Relative error (%)
1	1.0158 (mg)	1.2393 (mg)	18%
2	2.0641 (mg)	1.9695 (mg)	4.8%
3	2.9323 (mg)	2.6457 (mg)	10.8%
4	4.2409 (mg)	4.0297 (mg)	5.2%
5	5.3345 (mg)	5.9025 (mg)	9.6%

^a Using radioluminescence property of $Y_2O_3:Eu@SiO_2$.

Prior to any biological application, the cytotoxicity of the as-prepared $Y_2O_3:Eu@SiO_2$ was first assessed by an MTT assay. Different concentrations of $Y_2O_3:Eu@SiO_2$ were incubated with either CAOV3 or SKOV3 cells for 24 h in cell culture medium. As shown in **Figure S1**, at a concentration as high as 100 $\mu g mL^{-1}$, the cell viability of both CAOV3 and SKOV3 still remained above 90% after 24 h incubation with $Y_2O_3:Eu@SiO_2$, demonstrating the excellent biological

compatibility of $Y_2O_3:Eu@SiO_2$. As mentioned above, we have demonstrated that the X-ray irradiation of annealing-treated $Y_2O_3:Eu@SiO_2$ nanoparticles generated ROS *via* comprehensive photodynamic effects (both Type I and II). Consequently, we evaluated if the ability of the as-synthesized $Y_2O_3:Eu@SiO_2$ to generate ROS and induce cell damage after exposure to X-ray radiation which using both radio-sensitive (CAOV3) and radio-resistant (SKOV3) cell lines. As shown in **Figure 5**, untreated and $Y_2O_3:Eu@SiO_2$ treated CAOV3 cells exhibited negligible change in cell viability. Under X-ray irradiation, cells showed positive for PI staining within 3 h, as an indication of cell death, and the number of viable cells decreased after 24 h incubation. In contrast with CAOV3 cells, SKOV3 cells exhibited negligible change in cell viability in untreated, $Y_2O_3:Eu@SiO_2$, and X-ray alone groups. We postulate that these finding reflect that the radio-resistant SKOV3 cells eliminated the ROS by its intracellular repair capability [61]. The combined treatment showed cells with a positive signal for YO-PRO-1 at the initial phase (3 h), indicating changes in plasma membrane permeability. At the late phase (24 h), the majority of cells were positive for PI staining. These results demonstrated that our $Y_2O_3:Eu@SiO_2$ overcame the resistance of SKOV3 cells.

The destruction of tumor cells following X-ray irradiation of $Y_2O_3:Eu@SiO_2$ nanoparticles was determined by clonogenic assay, i.e., based upon the ability of a single cell to grow, post-treatment, into a colony. As shown in **Figure 6**, significant killing of both SKOV3 and CAOV3 cells was observed in the presence of $Y_2O_3:Eu@SiO_2$ nanoparticles with both 150 keV and 250 keV X-ray, and considerably more than with radiation alone. For the radiation-sensitive CAOV3 cells, the nanoparticles enhanced the therapeutic effect up to 40% in the 2 Gy of 150 keV X-ray. Most importantly, in the radio-resistant SKOV3 cells, more than 50% cell death was shown with $Y_2O_3:Eu@SiO_2$ nanoparticles at 2 Gy of 150 keV X-ray irradiation. The $Y_2O_3:Eu@SiO_2$ nanoparticles demonstrated significant therapeutic potential with lower dosage and energy X-ray irradiation in both radio-sensitive and resistant ovarian cancer cells.

Ovary is a radiosensitive tissue, and damage to ovary is of profound importance owing to the lack of repair of normal tissue and potentially severe sequelae. Because ovarian cancer is rarely confined to the pelvis, whole abdominal radiotherapy (WAR) was used to sterilize large volumes of micrometastatic intraperitoneal disease. Limited tolerance of the bowel, kidneys and liver also reduces the amount of radiation. Therefore, low-dose hyperfractionation could be considered as part of the standard

management for ovarian cancer [62-65]. Encouraged by the *in vitro* results, we further investigated an approach that is relevant to clinical stereotactic body radiation therapy: combination of radio-sensitization enhancement with a fractionated radiation regimen. Radiation was administered in four fractions of 8 Gy every other day (q1d×4) (**Figure 7A**). The effects of various treatments on the growth of subcutaneous SKOV3 tumors are shown in **Figure 7B**. The tumors in the control group progressively increased in size, which enlarged nearly by four-fold in tumor volume within 14 d. Compared with the aggravating increase tendency in the control group, either $Y_2O_3:Eu@SiO_2$ or X-ray radiation alone caused visible tumor growth delay within the first 4 d, accompanied by an approximately 25% and 50% tumor volume decrease at the end of 14 d, respectively. In the combination regimen, the tumor growth inhibition was enhanced; resulting in tumor growth stasis during the period of 25 d. Overall, tumor volume was delayed by five-fold compared to the control (474 mm³ vs. 2371 mm³). After 24 d, five of the six mice treated with $Y_2O_3:Eu@SiO_2$ and X-ray survived. The survival rates in those treated with X-ray alone, $Y_2O_3:Eu@SiO_2$ alone and control group were 66%, 0%, and 0%, respectively. (**Figure 7C**). No obvious toxicity was observed in the mice following $Y_2O_3:Eu@SiO_2$ administration, such as sudden death, abnormal behavior, significant changes of food in body weight. In addition, the histopathology examination confirmed that the structural patterns of major organs, including heart, liver, spleen, lung and kidney, of both the $Y_2O_3:Eu@SiO_2$ combined with X-ray irradiation group and X-ray alone group are similar to those of the control group. These results suggest that no obvious acute toxicity reaction was induced in the treatments (**Figure S2**).

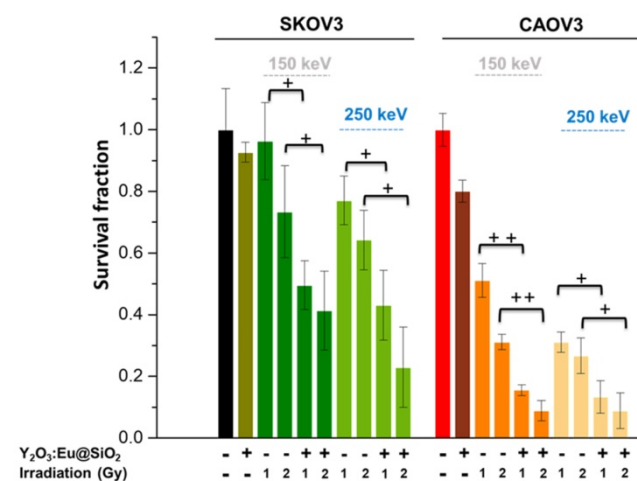


Figure 6. Survival of the ovarian cells for various tube voltages. Clonogenic survival assays of SKOV3 and CAOV3 cells treated with radiation alone or with $Y_2O_3:Eu@SiO_2$ incubation for 24 h followed by X-ray radiation, respectively.

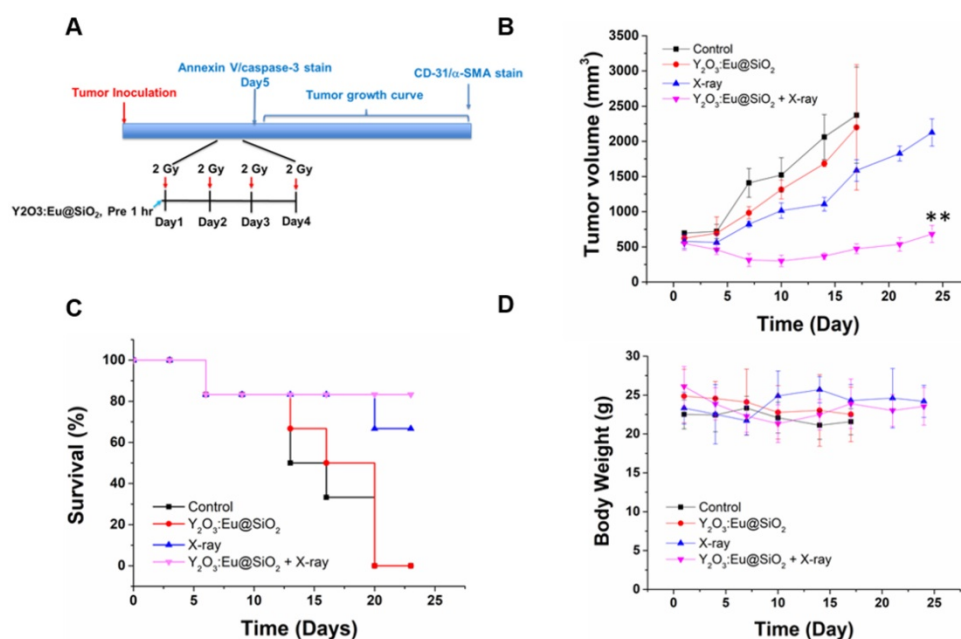


Figure 7. Synergistic effects on tumor growth delay with combined X-ray PDT and fractionated radiation therapy. (A) The treatment protocol for using hyperfractionated radiation therapy. (B) Radiosensitizing effect of $Y_2O_3:Eu@SiO_2$ combined with X-ray irradiation in nude mice bearing SKOV3 tumors. Tumor growths after treatments with PBS, 8 Gy irradiation, $Y_2O_3:Eu@SiO_2$ with or without 8 Gy irradiation. Each value represents the mean \pm SEM of tumor volume in mm^3 relative to that measured at the beginning of treatment. (C) Mouse survivals following various treatments. (D) The body weight of mice after various treatments.

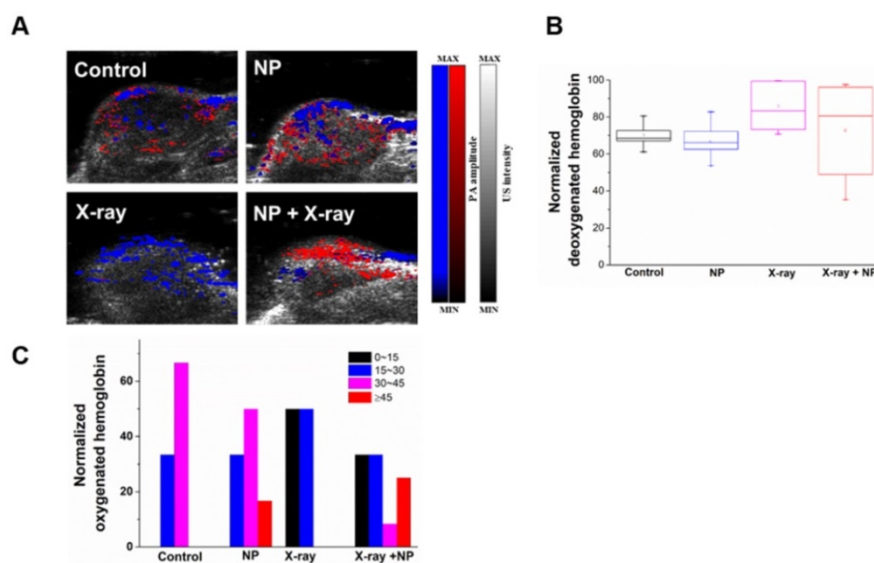


Figure 8. Validation of hypoxic conditions observed in photoacoustic images in vivo. (A) Oxygen saturation of a representative tumor cross-section profiled by photoacoustic image. (B) Mean deoxygenated hemoglobin of each group after X-ray irradiation. (C) Illustrations of the heterogeneous oxygenated hemoglobin distribution of different treatment groups.

It is well known that the response of tumor cells to radiation is closely related to oxygen supply through blood perfusion, and that fractionated radiotherapy minimizes radiation-induced vascular damage, thereby allowing reoxygenation of hypoxic tumor cells. To evaluate the contribution of $Y_2O_3:Eu@SiO_2$ presence to radiation dose enhancement and reoxygenation, photoacoustic imaging (PAI) was performed to discern oxygen saturation (sO_2) from the oxygenated and deoxygenated hemoglobin at different wavelengths of 850 and 750 nm, respectively [66-68]. As seen in

Figure 8A, the PAIs did not show any observable changes between the control and $Y_2O_3:Eu@SiO_2$ alone group. Furthermore, we noticed an unusual sO_2 decrease was found in the X-ray alone group after the treatment process. Surprisingly, the PAI in the combined group exhibited an observable increase in the sO_2 . This is of particular interest when considering potential applications of $Y_2O_3:Eu@SiO_2$ in X-ray PDT. Through measurement of sO_2 levels, the relative mean sO_2 showed a slight difference between the X-ray and the combined group (**Figure 8B**). Furthermore, the normalized sO_2 at the periphery of $Y_2O_3:Eu@SiO_2$

were obtained and quantified. It was found that the tumor treated with X-ray leads to a decrease of the sO_2 distribution (sO_2 was 50% at sO_2 0~15% and 50% at sO_2 15~30%), when compared to the control (sO_2 was 33.3% at sO_2 15~30% and 66.7% at sO_2 30~45%) and the $Y_2O_3:Eu@SiO_2$ alone groups (sO_2 was 33.3% at sO_2 15~30%, 50% at sO_2 30~45% and 16.7% at sO_2 \geq 45%) (**Figure 8C**). This phenomenon is in agreement with the extant literature [69], and is ascribed to endothelial death (with a threshold dose of 5~10 Gy) and a decrease in oxygen supply after X-ray irradiation. Moreover, Hasan et al. reported that PDT, as well as high single-dose radiation therapy, can create a temporal hypoxia region in tissue adjacent to perfused blood vessel [70]. This event might be expected to attenuate radiation therapy response. Additionally, an inadequate supply of O_2 (hypoxia) has long been recognized as a cause of radio-resistance, in which hypoxic tumor cells are approximately three times more resistant to radiotherapy (known as “the oxygen effect”). Interestingly, the $Y_2O_3:Eu@SiO_2$ with X-ray group showed enhanced sO_2 level at the periphery of tumor administered with $Y_2O_3:Eu@SiO_2$ (sO_2 was 33.3% at sO_2 0~15%, 33.3% at sO_2 15~30%, 8.4% at sO_2 30~40% and 25% at sO_2 \geq 45%). It could be reasonably speculate that, upon X-ray PDT, the oxygen demand in tumors is drastically diminished due to severe damage to tumor cells. On the other hand, the oxygen supply through blood perfusion continuously contributes to the intratumoral oxygen tension. Potiron et al. demonstrated that fractionated radiotherapy increased intratumoral doxorubicin diffusion [71]. These results are in accordance with Hansen et al., who reported that tumors displayed an increased mean accumulation of liposomes for radiation doses up to 10 Gy [72]. We observed obvious difference between the sO_2 values of the X-ray alone and the combined groups at 1 h post-X-ray PDT.

Induction of apoptosis in SKOV3 tumors at the end after various treatments is depicted in **Figure 9A**. As illustrated in **Figure 9A**, tumors treated with X-ray combined with $Y_2O_3:Eu@SiO_2$ showed the highest Annexin V expression, an early apoptosis marker, as compared to tumors with only X-ray irradiation and with $Y_2O_3:Eu@SiO_2$ alone. Moreover, the strongest caspase 3 signal was also observed in the group of X-ray combined with $Y_2O_3:Eu@SiO_2$, suggesting that $Y_2O_3:Eu@SiO_2$ effectively enhanced radiotherapy *via* cell apoptotic cascade. To explore other possible mechanisms besides apoptosis that synergistically contributed to the enhanced inhibition of tumor growth in the presence of our annealed $Y_2O_3:Eu@SiO_2$, we further assessed tumors harvested from various groups with immunofluorescence (IF) imaging of CD-31. The IF images showed a decrease in CD-31

positive endothelial cells at the end of treatment compared to the other groups (**Figure 9B**). Consistent with previous reports, high doses of radiation induced additional tumor cell killing through “non-classical” radiobiological mechanisms, mediated by tumor microvascular damage [73-75]. Specifically, Demidov et al. carried out longitudinal *in vivo* imaging observations, and demonstrated that maximal tumor shrinkage increases with dose, and the time to initial vascular volume density recovery is also dose-dependent. In our study, sO_2 in the combined group increases rapidly after irradiation, probably due to damage in the endothelial cells followed by widening of the gaps between endothelial cells. However, we also observed the vascular volume density declined at the end of treatment in combined group. Wang and colleagues reported copper-cysteamine NPs-mediated X-PDT, which caused a decrease in the number of vessels, but did not inhibit the growth of radio-resistant melanoma [76]. In our study, we demonstrated NP-mediated X-ray PDT combined with fractionated radiation therapy, which decreased the tumor vessels at the end of *in vivo* study. Further, multi-shots X-ray PDT treatment improved oxygen distribution at the periphery of tumor administered with $Y_2O_3:Eu@SiO_2$, and enhanced efficiency of X-ray to inhibit the growth of radio-resistant SKOV3. To further validate and assessed these findings, CD-31 and α -smooth muscle actin (α -SMA) stain was utilized to depict the vascular remodeling and pericyte recruitment. As shown in **Figure 9C**, a decrease in CD-31 (64%) intensity was found at the end of treatment compared to non-irradiated and NP alone tumors. Interestingly, in the X-ray alone group, an increase in α -SMA intensity was observed after three weeks of RT compared to non-irradiated (2.3-fold), NP alone (1.4-fold), and NPs combined with X-ray irradiated tumors (2.4-fold), indicating that the sublethal dose of irradiation could enhance radiotherapy-induced vascular remodeling at the late stage (**Figure 9D**). The X-ray induced vascular remodeling indexed with α -SMA was compromised in combined group is probably ascribed to the ROS generated by the annealed $Y_2O_3:Eu@SiO_2$ following X-ray irradiation, where the photoexcited electrons and holes of Y_2O_3 react with an aqueous electron acceptor (i.e., molecular oxygen) and donor (i.e., water and hydroxyl ions) to produce different types of ROS that abolish pericyte recruitment. Together, these findings implicate that annealed $Y_2O_3:Eu@SiO_2$ combined with fractionated radiation therapy has the potential to be utilized to reverse vascular remodeling-enhanced tumor resistance to radiation therapy.

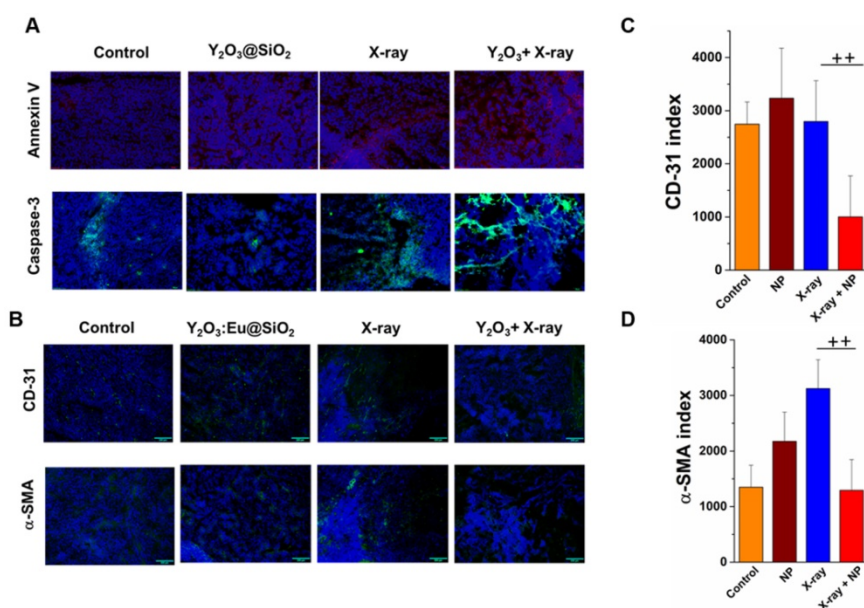


Figure 9. RT induces tumor redistribution and vascular damage. (A) Representative scanner images of immunohistochemistry for Annexin V and caspase-3 in SKOV3 tumors. (B) Representative scanner images of immunohistochemistry for endothelial cells (CD-31) and pericytes (α -SMA) for the different treatment groups after the four days radiation therapy. (C) (D) quantification of CD-31⁺ and α -SMA in SKOV3 tumor. Index values shown in (C) and (D) represent the mean of $n \geq 3 \pm$ SEM.

Conclusion

In summary, we have developed Y₂O₃:Eu@SiO₂ nanoscintillators that could be potentially used for X-RL imaging-guided radiotherapy with a significant radio-sensitization enhancement. It is notable that the annealing pretreatment is critical for Y₂O₃:Eu@SiO₂ to render such a PS-independent radio-sensitization enhancement that comprises comprehensive photodynamic effects and pronounced RL for possible imaging guidance and *in-situ* dosimetry assessment. This report further demonstrated that RL emission and ROS generation constitute two parallel and independent mechanisms, which is important as it implicates that the Y₂O₃:Eu@SiO₂ could harness the ionizing radiation efficiently to reach the maximal theranostic utilization. In imaging, the red-emitted X-RL of Y₂O₃:Eu@SiO₂ was quantitatively monitored for nanoparticle tumor accumulation and dosimeter assessment *in vivo*. However, in consideration of the penetration depth and scattering attribute of red X-RL in tissue, the quantitative dosimetry and imaging of Y₂O₃:Eu@SiO₂ are constrained to superficial tumors. We have demonstrated the ability of ROS generation of Y₂O₃:Eu@SiO₂ is independent of europium dopant ion concentration. Furthermore, due to the similar ionic radius of lanthanide ions to yttrium (for example, 1.933 Å for Yb, 1.761 Å for Er and 1.8 Å for Y), the challenge of producing high-penetration X-RL in our nanotheranostics may be addressed by substituting Eu³⁺ with other rare-earth-ions such as Yb³⁺ and Er³⁺ in the doping process, to possibly tuning and extending the peak emission wavelengths to near

infrared I and II regions. In addition, the generation of electron-hole pairs in Y₂O₃ could react with an aqueous electron acceptor (i.e., molecular oxygen) and donor (i.e., water and hydroxyl ions), which essentially minimize oxygen dependency for the generation of reactive oxygen species. Furthermore, for the *in-vivo* radio-sensitizing effect of our established nanoparticles, the preliminary results from tumor xenografts suggested that the therapeutic enhancement observed *in vivo* by Y₂O₃:Eu@SiO₂-derived radio-sensitization could be readily translated to favorable radiotherapy for tumor control. A new indication is noteworthy that Y₂O₃:Eu@SiO₂ in combination with fractionated radiation therapy could induce vascular remodeling that accompanied by decreased hypoxia distribution intratumorally. It is anticipated to alleviate the radiobiological effect associated with tumor radioresistance and to substantially improve conventional PDT.

Supplementary Material

Supplementary figures and tables.

<http://www.thno.org/v10p6758s1.pdf>

Acknowledgement

This work was financially supported by research funds collectively from MOST 105-2113-M-400-007-MY3 (Ministry of Science and Technology of Taiwan) and 06A1-PP04-014 (National Health Research Institutes of Taiwan). We would also like to acknowledge the assistance in proof editing provided by Dr. Jeffery S. Souris in Department of Radiology,

The University of Chicago, USA, and Dr. Maharajan Sivasubramanian in Institute of Biomedical Engineering and Nanomedicine, National Health Research Institutes, Taiwan.

Competing Interests

The authors have declared that no competing interest exists.

References

- Dolmans DEJGJ, Fukumura D, Jain RK. Photodynamic therapy for cancer. *Nat. Rev. Cancer*. 2003; 3:380-7.
- Robertson CA, Evans DH, Abrahamse H. Photodynamic therapy (PDT): A short review on cellular mechanisms and cancer research applications for PDT. *J Photochem Photobiol B*. 2009; 96:1-8.
- Mallidi S, Anbil S, Bulin AL, Obaid G, Ichikawa M, Hasan T. Beyond the barriers of light penetration: Strategies, perspectives and possibilities for photodynamic therapy. *Theranostics*. 2016; 6:2458-87.
- Ethirajan M, Chen Y, Joshi P, Pandey RK. The role of porphyrin chemistry in tumor imaging and photodynamic therapy. *Chem Soc Rev*. 2011; 40:340-62.
- Wang C, Cheng L, Liu Z. Upconversion nanoparticles for photodynamic therapy and other cancer therapeutics. *Theranostics*. 2013; 3:317-30.
- Sivasubramanian M, Chuang YC, Lo LW. Evolution of nanoparticle-mediated photodynamic therapy: From superficial to deep-seated cancers. *Molecules*. 2019; 24:1-17.
- Cheng L, Wang C, Feng L, Yang K, Liu Z. Functional nanomaterials for phototherapies of cancer. *Chem Rev*. 2014; 114:10869-939.
- Lucky SS, Soo KC, Zhang Y. Nanoparticles in photodynamic therapy. *Chem Rev*. 2015; 115:1990-2042.
- Wu X, Chen G, Shen J, Li Z, Zhang Y, Han G. Upconversion nanoparticles: A versatile solution to multiscale biological imaging. *Bioconjug Chem*. 2015; 26:166-75.
- Cheng SH, Hsieh CC, Chen NT, Chu CH, Huang CM, Chou PT, et al. Well-defined mesoporous nanostructure modulates three-dimensional interface energy transfer for two-photon activated photodynamic therapy. *Nano Today*. 2011; 6:552-63.
- Chen NT, Tang KC, Chung MF, Cheng SH, Huang CM, Chu CH, et al. Enhanced plasmonic resonance energy transfer in mesoporous silica-encased gold nanorod for two-photon-activated photodynamic therapy. *Theranostics*. 2014; 4:798-807.
- Tian G, Gu Z, Zhou L, Yin W, Liu X, Yan L, et al. Mn²⁺ dopant-controlled aynthesis of NaYF₄:Yb/Er upconversion nanoparticles for *in vivo* imaging and drug delivery. *Adv Mater*. 2012; 24:1226-31.
- Kamkaew A, Chen F, Zhan Y, Majewski RL, Cai W. Scintillating nanoparticles as energy mediators for enhanced photodynamic therapy. *ACS Nano*. 2016; 10:3918-35.
- Chu X, Mao L, Johnson O, Li K, Phan J, Yin Q, et al. Exploration of TiO₂ nanoparticle mediated microdynamic therapy on cancer treatment. *Nanomedicine*. 2019; 272-81.
- Yao M, Ma L, Li L, Zhang J, Lim Rx, Chen W, et al. A new modality for cancer treatment—Nanoparticle mediated microwave induced photodynamic therapy. *J Biomed Nanotechnol*. 2016; 12:1835-51.
- Canavese G, Ancona A, Racca L, Canta M, Dumontel B, Barbaresco F, Limongi T, Cauda V. Nanoparticle-assisted ultrasound: A special focus on sonodynamic therapy against cancer. *Chem Eng J*. 2018; 340:155-172.
- Dou Y, Liu Y, Zhao F, Guo Y, Li X, Wu M, et al. Radiation-responsive scintillating nanotheranostics for reduced hypoxic radioresistance under ROS/NO-mediated tumor microenvironment regulation. *Theranostics*. 2018; 8:5870-89.
- Shrestha S, Wu J, Sah B, Vanasse A, Cooper LN, Ma L, et al. X-ray induced photodynamic therapy with copper-cysteamine nanoparticles in mice tumors. *Proc Natl Acad Sci USA*. 2019; 116:16823-16828.
- Sun W, Zhou Z, Pratz G, Chen X, Chen H. Nanoscintillator-mediated X-ray induced photodynamic therapy for deep-seated tumors: From concept to biomedical applications. *Theranostics*. 2020; 10:1296-318.
- Chen W, Zhang J. Using nanoparticles to enable simultaneous radiation and photodynamic therapies for cancer treatment. *J Nanosci Nanotechnol*. 2006; 6:1159-66.
- Kotagiri N, Sudlow GP, Akers WJ, Achilefu S. Breaking the depth dependency of phototherapy with Cerenkov radiation and low radiance responsive nanophotosensitizers. *Nat Nanotechnol*. 2015; 10: 370-379.
- Clement S, Deng W, Camilleri E, Wilson BC, Goldys EM. X-ray induced singlet oxygen generation by nanoparticle-photosensitizer conjugates for photodynamic therapy: Determination of singlet oxygen quantum yield. *Sci Rep*. 2016; 6:19954.
- Tang Y, Hu J, Elmenoufy AH, Yang X. Highly efficient FRET system capable of deep photodynamic therapy established on x-ray excited mesoporous LaF₃:Tb scintillating nanoparticles. *ACS Appl Mater Interfaces*. 2015; 7:12261-9.
- Wang GD, Nguyen HT, Chen H, Cox PB, Wang L, Nagata K, et al. X-ray induced photodynamic therapy: A combination of radiotherapy and photodynamic therapy. *Theranostics*. 2016; 6:2295-305.
- Dougherty TJ. Photosensitizers: Therapy and detection of malignant tumors. *Photochem Photobiol*. 1987; 45:879-89.
- Zou X, Yao M, Ma L, Hossu M, Han X, Juzenas P, et al. X-ray-induced nanoparticle-based photodynamic therapy of cancer. *Nanomedicine*. 2014; 9:2339-51.
- Chen H, Rogalski MM, Anker JN. Advances in functional x-ray imaging techniques and contrast agents. *Phys Chem Chem Phys*. 2012; 14:13469-86.
- Kiracki K, Kubat P, Fejfarova K, Martincik J, Nikl M, Lang K. X-ray inducible luminescence and singlet oxygen sensitization by an octahedral molybdenum cluster compound: A new class of nanoscintillators. *Inorg Chem*. 2016; 55:803-9.
- Henderson BW, Busch TM, Snyder JW. Fluence rate as a modulator of PDT mechanisms. *Lasers Surg Med*. 2006; 38:489-93.
- Chen H, Wang GD, Chuang YJ, Zhen Z, Chen X, Biddinger P, et al. Nanoscintillator-mediated x-ray inducible photodynamic therapy for *in vivo* cancer treatment. *Nano letters*. 2015; 15:2249-56.
- Huang Z, Chen Q, Shakil A, Chen H, Beckers J, Shapiro H, et al. Hyperoxygenation enhances the tumor cell killing of photofrin-mediated photodynamic therapy. *Photochem Photobiol*. 2003; 78:496-502.
- Jarvi MT, Niedre MJ, Patterson MS, Wilson BC. Singlet oxygen luminescence dosimetry (SOLD) for photodynamic therapy: Current status, challenges and future prospects. *Photochem Photobiol*. 2006; 82:1198-210.
- Zhang C, Zhao K, Bu W, Ni D, Liu Y, Feng J, et al. Marriage of scintillator and semiconductor for synchronous radiotherapy and deep photodynamic therapy with diminished oxygen dependence. *Angew Chem Int Ed Engl*. 2015; 54:1770-4.
- Toma-Dasu I, Sandström H, Barsoum P, Dasu A. To fractionate or not to fractionate? That is the question for the radiosurgery of hypoxic tumors. *J Neurosurg*. 2014; 121:110-5.
- Souris JS, Cheng SH, Pelizzari C, Chen NT, La Riviere P, Chen CT, et al. Radioluminescence characterization of in situ x-ray nanodosimeters: Potential real-time monitors and modulators of external beam radiation therapy. *Appl Phys Lett*. 2014; 105: 203110.
- Chang M, Tie S. Fabrication of novel luminor Y₂O₃:Eu³⁺@SiO₂@YVO₄:Eu³⁺ with core/shell heteronanostructure. *Nanotechnology*. 2008; 19:075711.
- He W, Liu Y, Wamer WG, Yin JJ. Electron spin resonance spectroscopy for the study of nanomaterial-mediated generation of reactive oxygen species. *J Food Drug Anal*. 2014; 22:49-63.
- Misawa M, Takahashi J. Generation of reactive oxygen species induced by gold nanoparticles under x-ray and UV irradiations. *Nanomedicine*. 2011; 7:604-14.
- Kolemen S, Ozdemir T, Lee D, Kim GM, Karatas T, Yoon J, et al. Remote-controlled release of singlet oxygen by the plasmonic heating of endoperoxide-modified gold nanorods: Towards a paradigm change in photodynamic therapy. *Angew Chem Int Ed Engl*. 2016; 55:3606-10.
- Lai P, Xu X, Wang LV. Dependence of optical scattering from Intralipid in gelatin-gel based tissue-mimicking phantoms on mixing temperature and time. *J Biomed Opt*. 2014; 19:35002.
- Kai C, Chao G, Bo P, Wei W. The influence of SiO₂ shell on fluorescent properties of LaF₃:Nd³⁺ /SiO₂ core/shell nanoparticles. *J Nanomater*. 2010; 5:1-6.
- Xie D, Peng H, Huang S, You F. Core-shell structure in doped inorganic nanoparticles: approaches for optimizing luminescence properties. *J Nanomater*. 2013; 891515.
- Sahay G, Alakhova DY, Kabanov AV. Endocytosis of nanomedicines. *J Control Release*. 2010; 145:182-95.
- Gan Q, Dai D, Yuan Y, Qian J, Sha S, Shi J, et al. Effect of size on the cellular endocytosis and controlled release of mesoporous silica nanoparticles for intracellular delivery. *Biomed Microdevices*. 2012; 14:259-70.
- Gupta BK, Narayanan TN, Vithayathil SA, Lee Y, Koshy S, Reddy AL, et al. Highly luminescent-paramagnetic nanophosphor probes for *in vitro* high-contrast imaging of human breast cancer cells. *Small*. 2012; 8:3028-34.
- Molina P, Sommer M, Kattner F, Henniger J. Response characterization of an Y₂O₃:Eu-based radioluminescence probe under ⁶⁰Co irradiation. *Radiat Meas*. 2013; 56:338-41.

47. Yang J, Quan Z, Kong D, Liu X, Lin J. $Y_2O_3:Eu^{3+}$ microspheres: Solvothermal synthesis and luminescence properties. *Cryst. Growth Des.* 2007; 7:730-5.
48. Yan T, Zhang D, Shia L, Yang H, Mai H, Fang J. Reflux synthesis, formation mechanism, and photoluminescence performance of monodisperse $Y_2O_3:Eu^{3+}$ nanospheres. *Mater. Chem. Phys.* 2009; 117:234-43.
49. Hou X, Zhou S, Li Y, Li W. Luminescent properties of nano-sized $Y_2O_3:Eu$ fabricated by co-precipitation method. *J. Alloys Compd.* 2010; 494:382-5.
50. Pi D, Wang F, Fan X, Wang M, Zhang Y. Luminescence behavior of Eu^{3+} doped LaF_3 nanoparticles. *Spectrochim Acta A Mol Biomol Spectrosc.* 2005; 61:2455-9.
51. Xiao Y, Wu D, Jiang Y, Liu N, Liu J, Jiang K. Nano-sized $Y_2O_3:Eu^{3+}$ hollow spheres with enhanced photoluminescence properties. *J. Alloys Compd.* 2011; 509:5755-60.
52. Krylova G, Dimitrijevic NM, Talapin DV, Guest JR, Borchert H, Lobo A, et al. Probing the surface of transition-metal nanocrystals by chemiluminescence. *J Am Chem Soc.* 2010; 132:9102-10.
53. Lu Q, Li A, Guo F, Sun L, Zhao L. The two-photon excitation of SiO_2 -coated $Y_2O_3:Eu^{3+}$ nanoparticles by a near-infrared femtosecond laser. *Nanotechnology.* 2008; 19:205704.
54. Ju X, Li X, Yang Y, Li W, Tao C, Feng W. Luminescence properties of core-shell structured $SiO_2@CaMoO_4:Eu^{3+}$ phosphor. *J Solid State Chem.* 2012; 187:109-13.
55. Ansari AA, Parchur AK, Alam M, Azzeer A. Effect of surface coating on optical properties of Eu^{3+} -doped $CaMoO_4$ nanoparticles. *Spectrochim. Acta A.* 2014; 131:30-6.
56. Qian HS, Guo HC, Ho PC, Mahendran R, Zhang Y. Mesoporous-silica-coated upconversion fluorescent nanoparticles for photodynamic therapy. *Small.* 2009; 5:2285-90.
57. Ogorodnikov IN, Kruzhalov AV, Ivanov VY. Mechanisms of fast UV-scintillations in oxide crystals with self-trapped excitons. In *Inorganic scintillators and their applications*; felt University Press (SCINT95); Amsterdam, The Netherlands, 1996; 216-9.
58. Scaffidi JP, Gregas MK, Lauly B, Zhang Y, Vo-Dinh T. Activity of psoralen-functionalized nanoscintillators against cancer cells upon x-ray excitation. *ACS Nano.* 2011; 5:4679-87.
59. Li Y, Zhang W, Niu J, Chen Y. Mechanism of photogenerated reactive oxygen species and correlation with the antibacterial properties of engineered metal-oxide nanoparticles. *ACS Nano.* 2012; 6:5164-73.
60. Ravishankar TN, de Oliveira Vaz M, Khan S, Ramakrishnappa T, Teixeira SR, Balakrishna GR, et al. Enhanced photocatalytic hydrogen production from Y_2O_3/TiO_2 nano-composites: A comparative study on hydrothermal synthesis with and without an ionic liquid. *New J Chem.* 2016; 40:3578-87.
61. Miladi I, Aloy MT, Armandy E, Mowat P, Kryza D, Magne N, et al. Combining ultrasmall gadolinium-based nanoparticles with photon irradiation overcomes radioresistance of head and neck squamous cell carcinoma. *Nanomedicine.* 2015; 11:247-57.
62. Albuquerque KV, Singla R, Potkul RK, Smith DM, Creech S, Lo S, et al. Impact of tumor volume-directed involved field radiation therapy integrated in the management of recurrent ovarian cancer. *Gynecol Oncol.* 2005; 96:701-4.
63. Stephen F. Principles of cancer treatment by radiotherapy. *Surgery.* 2006; 24:62-5.
64. Machida S, Takei Y, Yoshida C, Takahashi Y, Koyanagi T, Sato N, et al. Radiation therapy for chemotherapy-resistant recurrent epithelial ovarian cancer. *Oncology.* 2014; 86:232-8.
65. Fields EC, McGuire WP, Lin L, Temkin SM. Radiation treatment in women with ovarian Cancer: Past, present, and future. *Front Oncol.* 2017; 7:177.
66. Bandla A, Liao LD, Chan SJ, Ling JM, Liu YH, Shih YI, et al. Simultaneous functional photoacoustic microscopy and electrocorticography reveal the impact of rtPA on dynamic neurovascular functions after cerebral ischemia. *J Cereb Blood Flow Metab.* 2018; 38:980-995.
67. Liu YH, Chan SJ, Pan HC, Bandla A, King NKK, Wong PTH, et al. Integrated treatment modality of cathodal-transcranial direct current stimulation with peripheral sensory stimulation affords neuroprotection in a rat stroke model. *Neurophotonics.* 2017; 4:045002.
68. Liao LD, Li ML, Lai HY, Shih YY, Lo YC, Tsang S, et al. Imaging brain hemodynamic changes during rat forepaw electrical stimulation using functional photoacoustic microscopy. *Neuroimage.* 2010; 52:562-70.
69. Fuks Z, Kolesnick R. Engaging the vascular component of the tumor response. *Cancer Cell.* 2005; 8:89-91.
70. Mallidi S, Watanabe K, Timerman D, Schoenfeld D, Hasan T. Prediction of tumor recurrence and therapy monitoring using ultrasound-guided photoacoustic imaging. *Theranostics.* 2015; 5:289-301.
71. Potiron V, Clément-Colmou K, Jouglar E, Pietri M, Chiavassa S, Delpon G, et al. Tumor vasculature remodeling by radiation therapy increases doxorubicin distribution and efficacy. *Cancer Lett.* 2019; 457:1-9.
72. Hansen AE, Fliedner FP, Henriksen JR, Jørgensen JT, Clemmensen AE, Børresen B, et al. Liposome accumulation in irradiated tumors display important tumor and dose dependent differences. *Nanomedicine.* 2018; 14:27-34.
73. Park HJ, Griffin RJ, Hui S, Levitt SH, Song CW. Radiation-induced vascular damage in tumors: Implications of vascular damage in ablative hypofractionated radiotherapy (SBRT and SRS). *Radiat Res.* 2012; 177:311-27.
74. Song C, Hong BJ, Bok S, Lee CJ, Kim YE, Jeon SR, et al. Real-time tumor oxygenation changes after single high-dose radiation therapy in orthotopic and subcutaneous lung cancer in mice: Clinical implication for stereotactic ablative radiation therapy schedule optimization. *Int J Radiat Oncol Biol Phys.* 2016; 95:1022-31.
75. Demidov V, Maeda A, Sugita M, Madge V, Sadanand S, Fluerau C, et al. Preclinical longitudinal imaging of tumor microvascular radiobiological response with functional optical coherence tomography. *Sci Rep.* 2018; 8:38.
76. Shi L, Liu P, Wu J, Ma L, Zheng H, Antosh MP, et al. The effectiveness and safety of X-PDT for cutaneous squamous cell carcinoma and melanoma. *Nanomedicine (Lond).* 201; 14:2027-43.